

TRACING THE PHYSICAL CONDITIONS IN ACTIVE GALACTIC NUCLEI WITH TIME-DEPENDENT CHEMISTRY

ROWIN MEIJERINK¹, MARCO SPAANS¹, INGA KAMP¹, GIAMBATTISTA ARESU¹, WING-FAI THI², AND PETER WOITKE³

¹ University of Groningen, Kapteyn Astronomical Institute, Postbus 800, 9700 AV, Groningen, The Netherlands

² UJF-Grenoble, CNRS-INSU, Institute de Planétologie et d'Astrophysique (IPAG) UMR 5274 and

³ SUPA, School of Physics and Astronomy, University of St. Andrews, KY16 9SS, UK

Draft version September 11, 2018

ABSTRACT

We present an extension of the code ProDiMo that allows for a modeling of processes pertinent to active galactic nuclei and to an ambient chemistry that is time dependent. We present a proof-of-concept and focus on a few astrophysically relevant species, e.g., H^+ , H_2^+ and H_3^+ ; C^+ and N^+ ; C and O ; CO and H_2O ; OH^+ , H_2O^+ and H_3O^+ ; HCN and HCO^+ . We find that the freeze-out of water is strongly suppressed and that this affects the bulk of the oxygen and carbon chemistry occurring in AGN. The commonly used AGN tracer HCN/HCO^+ is strongly time-dependent, with ratios that vary over orders of magnitude for times longer than 10^4 years. Through ALMA observations this ratio can be used to probe how the narrow-line region evolves under large fluctuations in the SMBH accretion rate. Strong evolutionary trends, on time scales of $10^4 - 10^8$ years, are also found in species such as H_3O^+ , CO , and H_2O . These reflect, respectively, time dependent effects in the ionization balance, the transient nature of the production of molecular gas, and the freeze-out/sublimation of water.

Subject headings: astrochemistry – galaxies: starburst – galaxies: active – interstellar medium

1. INTRODUCTION

Actively star-forming galaxies, like ultra-luminous infrared galaxies (ULIRGs), are generally highly obscured and may host an accreting super-massive black hole (SMBH). Observations at optical, UV, and X-ray wavelengths do not allow one to probe the inner regions of these systems. This is possible at far-infrared and millimeter wavelengths, though. A major step forward is being made with the current generation of ground and space based telescopes. The Herschel Space Observatory probes the window at wavelengths ranging from $\lambda = 50$ and $600 \mu m$ that is blocked by the Earth's atmosphere. It contains CO and H_2O transitions that are suitable to diagnose the gas chemical and thermal properties. These are affected by ultra-violet and X-ray photons, which are emitted by newly formed stars and the central SMBH. High spatial resolution (better than a few pc) observations of the molecular gas around an active galactic nucleus (AGN) have not been possible yet, but progress is foreseen when the Atacama Large Millimeter Array (ALMA) becomes fully functional in 2013. This array will consist of 66 telescope dishes, and will observe on scales smaller than one parsec in the nearest active galaxies, resolving at least the narrow line region around the SMBH.

One of the lessons learned from the Science Demonstration Phase of Herschel was that the presence of both SMBH accretion and star formation in Mrk 231 can be deduced from the CO spectral line energy distribution (SLED). A SPIRE FTS spectrum with CO lines up to $J=13-12$ between wavelengths $\lambda = 303 - 670 \mu m$ (van der Werf et al. 2010) was obtained within the Open Time Key Program HerCULES (PI: Van der Werf). The spectrum shows CO , $[CI]$, and $[NII]$ lines,

and surprisingly also strong lines of H_2O and the ionic species OH^+ and H_2O^+ . For the interpretation they used UV and X-ray dominated semi-infinite slabs models (Meijerink & Spaans 2005; Meijerink et al. 2007). These models calculate the thermal and chemical balance of gas irradiated by UV or X-rays, and predict the molecular emission of, e.g., CO and H_2O . They showed that the excitation of the CO ladder in the circumnuclear molecular disk (CMD) is dominated by the nuclear X-ray radiation field, out to a radius of ~ 160 pc. In a companion paper (González-Alfonso et al. 2010) the modeling was done for the H_2O lines and the conclusions was that the gas excitation and chemistry in Mrk 231 is by affected shocks/cosmic rays, an XDR chemistry, and/or an “undepleted chemistry” where grain mantles are evaporated.

Although some lessons were drawn from the model results for Mrk 231, it is not satisfactory to need separate modeling for, e.g., the CO and H_2O lines. Also, we would like to extract more information than ambient densities and radiation field strengths, such as the spatial origin of the different observed lines. Therefore, it is required to make more sophisticated models, which are able to deal with (1) the new inventory of diagnostic lines obtained with Herschel and (2) the high spatial resolution data from ALMA. Such a model should consider the geometry of the system that consists of gas, stars and an accreting SMBH in a single simulation. Indeed, the narrow-line region has a (puffed-up) disk structure with the radiation from the broad-line region very close to the SMBH impinging under a range of angles. Our aim in this work is to provide such a model, but also one that is fast enough to allow for a large parameter study, such that it can be used by the scientific community to understand the nature of the ISM located in the centers of nearby and high redshift, active galaxies.

The chemical relaxation timescales (see the section on chemical relaxation timescales below for the precise defi-

niton we adopted) in the UV and X-ray exposed warm, partly molecular layer are typically of order 10^4 yrs and can be as short as $\sim 1 - 100$ yrs for highly ionized gas, $x_e \sim 1$, and moderate densities $n > 10^3 - 10^4 \text{ cm}^{-3}$. The chemical relaxation timescale in the regions where the ISM is shielded from both UV and X-ray radiation ($A_V \gg 1$ and $\tau(1\text{keV}) \gg 1$, see Fig. 6) can be as large as 10^8 yrs. These long timescales will occur at low dust and gas temperatures, and requires that both FUV and X-ray ionization and heating are greatly reduced from its initial value. Here, the gas is slowly freezing out on dust grains, yielding a slow grain-surface chemistry. These timescales are larger than the typical dynamical (orbital) timescales of $\tau_{\text{dyn}} < 10^6 - 10^7$ years at < 100 pc from a $> 10^7 M_\odot$ SMBH with a surrounding torus of $\sim 10^9 M_\odot$, while supernova are expected to stir up the medium on timescales of $\tau_{\text{SN}} \sim 10^4$ yrs (Wada et al. 2009); a duration over which one would expect significant changes in the (column) density, gas kinematics and irradiation of orbiting molecular clouds. Work on AGN (Wada et al. 2009; Pérez-Beaupuits et al. 2011) has shown that an inhomogeneous swelled-up disk (on a 10 pc scale) is created by supernovae, with interstellar material transiting in between cold/dense and warm/diffuse phases on a dynamical time, while enjoying a range in UV and X-ray irradiations. Furthermore, supernova explosions, aided by a possible outflow, can drive shocks and cloud-cloud collisions that affect the gas phase chemistry and cause sputtering/evaporation of dust grains, releasing their icy mantles.

In light of the above, it is therefore likely that H_2O , crucial in interstellar chemistry, is not entirely frozen out in dense clouds. Also, important species like CO and H_2 may not be in chemical equilibrium, while ion-molecule chemistry (e.g., C^+ , OH^+ , HCO^+) can be boosted by large fluctuations in ionization rate. All these effects strongly alter the chemistry in the narrow line region and thus the interpretation of observations that use molecules to probe, a.o., the accretion flow towards the SMBH, the nature of star formation in AGN, and the importance of mechanical and radiative feedback. To make progress in this field, it is thus necessary to calculate the disk thermal and chemical balance as a function of time.

In this paper, as a first proof-of-concept step, we present a two-dimensional cylindrically symmetric thermal and chemical model with a parametrized distribution of gas and stars around a SMBH. We first calculate the equilibrium thermal and chemical structure for a generic model, and show that the chemical relaxation timescale in the regions where the gas is cold ($T < 50$ K) and molecular ($x_{\text{H}_2} \sim 0.5$) is of order 10^8 yrs, and completely depleted from CO and H_2O . Given the dynamical and supernova timescale described above, it is expected that the chemistry is not in equilibrium and that grains are (partially) stripped from their ice-layers. Therefore, we follow up with a calculation in which we follow the chemical relaxation of the gas phase and surface chemistry. In that calculation the thermal and hydrostatic structure is fixed. We compare the chemical structures of the equilibrium and time-dependent solutions, and discuss the implications on the observed line emission. This model is calculated using a modified version of the ProDiMo (Woitke et al. 2009, 2011) (Protoplanetary Disk Model),

that has been developed originally to interpret observations of protoplanetary disks around newly formed T Tauri and Herbig Ae/Be stars.

2. MODIFYING THE PRODIMO CODE TO BLACK HOLE ENVIRONMENTS

The original ProDiMo code is a code that is used to study the physical, chemical and thermal structure of gas and dust around T Tauri and Herbig Ae/Be stars. The original code includes (1) frequency dependent continuum radiative transfer (2) kinetic gas-phase and FUV photochemistry, (3) ice-formation, and (4) detailed non-local thermodynamic equilibrium (non-LTE) heating and cooling with (5) a consistent calculation of the hydrostatic disk structure. The models are characterized by a high degree of consistency among the various physical, chemical, and radiative processes, since the mutual feedbacks are solved iteratively. X-ray heating and chemical processes are included, based on work of several authors (Maloney et al. 1996; Glassgold et al. 2004; Meijerink & Spaans 2005). It includes the most recent X-ray physics (Ádámkóvics et al. 2011) with an extension of the chemical network with species such as Ne, Ar, and their doubly and singly ionized species, as well as other heavy elements.

The model makes predictions of observables such as [CII] and [OI] fine-structure lines, rotational lines of CO, and ro-vibrational lines of H_2O , using an escape probability method (Woitke et al. 2011). The code is set-up in a modular way. It allows to use either a prescribed density structure, or to calculate the hydrostatic structure self-consistently with the thermal-chemical structure. A full parametrization of the structure is important to calculate large model grids, while the self-consistent structure is more appropriate in the case of detailed model for a specific object. Examples are the modeling of HD 163296 (Tilling et al. 2012) and a large grid with 300000 models (Woitke et al. 2011). In two recent papers, discussing a grid of 240 models, the combined effects of X-ray and FUV radiation on the disk physical structure were calculated for a range of radiation fields, dust properties and surface density profiles (Meijerink et al. 2012a) and the statistical properties of diagnostic gas lines were studied (Aresu et al. 2012). The code allows to start from a converged physical structure solution and then evolve the chemistry in time after, e.g., changing the input spectrum.

3. THE GENERIC TORUS MODEL

We scaled up the ProDiMo models in such a way that they represent the circumnuclear molecular disk (CMD) around an accreting black hole. Currently, supernova feedback and radiation pressure are not included. For this reason, we do not use the iteration of global disk structure to reach hydrostatic equilibrium, but we define a pre-prescribed density structure, with a power law surface density distribution, $\Sigma \propto R^{-1}$. The density distribution is decoupled from the thermal structure of the torus, implicitly assuming that the vertical scale-height is maintained by non-thermal processes, such as turbulent motions. These turbulent motions would result in a clumpy density structure, which is beyond the scope of this paper and therefore not taken into account. The penetration depth of especially UV (and to a lesser ex-

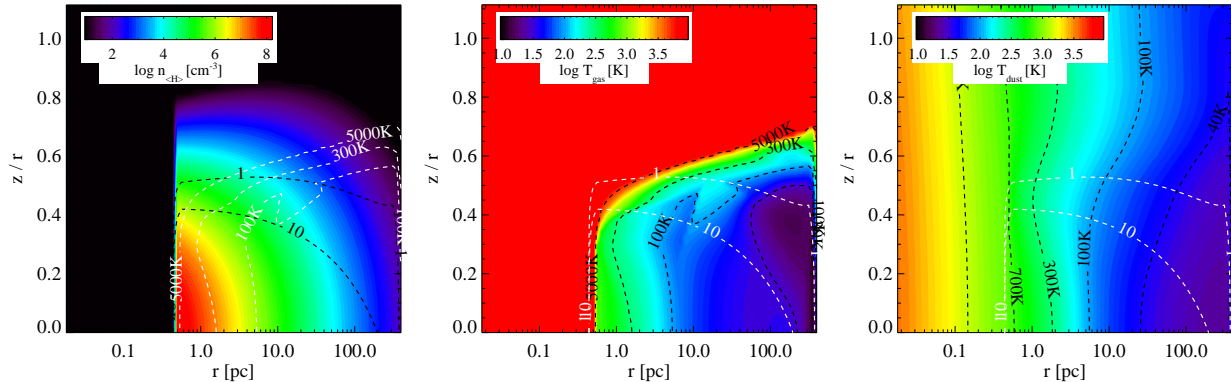


FIG. 1.— Gas number density (left), and gas temperature (middle) and dust temperature (right) for a model with disk mass $M_{\text{disk}} = 10^9 M_{\odot}$ and $L_X = 10^{43} \text{ erg s}^{-1}$. The visual extinction $A_V = 1$ and 10 and temperatures $T_{\text{gas}} = 100, 300$ and 5000 K are indicated with contours. Note: The vertical axis depicts the relative height, allowing a better visualization of the inner regions.

tent X-rays that have a lower absorption cross section) is on average larger in a clumpy structure, and would result in a less stratified structure (Spaans 1996). Our generic torus model has a gas mass, $M_{\text{disk}} = 10^9 M_{\odot}$, which is in the range of gas masses found for ULIRGs in the nearby universe (Papadopoulos et al. 2012). We set the inner radius $R_{\text{in}} = 0.5 \text{ pc}$, and outer radius $R_{\text{out}} = 400 \text{ pc}$, the latter being comparable to the inner disk size found with interferometric imaging of CO $J = 1 - 0$ and $J = 2 - 1$ for Mrk 231 (Downes & Solomon 1998). We note here that “torus” is used in a broad sense here, given that the outer radius is three orders of magnitude larger than the inner radius of the model. This dynamical range implies that this torus is not meant to be seen as a cohesive structure. The scale height is $H_0 = 0.5 \text{ pc}$ at a reference radius of 3.0 pc . This gives a puffed up disk, as suggested by numerical simulations (Wada et al. 2009). The total luminosity of the central source is $L = 10^{10} L_{\odot}$. The X-ray luminosity between 0.1 and 10 keV of the accreting black hole is $L_X = 10^{43} \text{ erg s}^{-1}$, which is a typical luminosity for a sample of local Syfert 1 and 2 galaxies (Lutz et al. 2004), and has a power law distribution with index $\beta = -0.9$. The disk has a flaring index of $\alpha = 1.1$ (where flaring implies the increase of $H(r)/r$ with radius). The global interstellar radiation field is set to $\chi = 10^3$ (the Draine field (Draine 1978)). This is representing the additional radiation in the UV produced by the stars in the AGN environment. It needs to be pointed out that the impact of the UV, and especially that originating from the nucleus, on the molecular part of the torus is small, since most of the UV is already absorbed given the large A_V . The cosmic ray ionization rate to $\zeta = 5 \times 10^{-17} \text{ s}^{-1}$. Below, we will discuss the results for an equilibrium solution and a time-dependent solution. We would like to point out that although these parameters are chosen in such a way that they are representative for a typical AGN, but that it is still a proof of concept paper. A study varying parameters such as the torus mass, and UV and X-ray luminosities from the central source and the stars, is postponed to another paper.

3.1. The equilibrium solution

Density and temperatures: density and gas and dust temperature structures are shown for a generic disk (Fig. 1). To guide the eye, we overplot $A_V = 1$ and 10, which

is defined as the smallest optical depth in either the vertical or radial direction toward the ‘surface’ of the torus. The FUV radiation is dominated by the central source, when the visual extinction is smallest in the radial direction, dominated by the stellar radiation field when it is smallest in the vertical direction. Densities range from $n_{\text{H}} < 10 \text{ cm}^{-3}$ at large altitudes in the disk, to $n_{\text{H}} = 10^8 \text{ cm}^{-3}$ at the mid-plane ($z/r \sim 0$) and close to the inner rim ($r \sim 0.5 \text{ pc}$) of the disk. The gas temperature is decoupled from the dust temperature, except for the regions of the disk where densities are high $n = 10^5 - 10^8 \text{ cm}^{-3}$, and both the UV and X-ray radiation field is largely attenuated. The unshielded parts of the disk show gas temperatures $T > 5000 \text{ K}$, much larger than the dust temperatures, which range from $T \sim 40 - 1400 \text{ K}$ in the same region. Figure 1 shows a contour where the dust temperature is $T_{\text{dust}} = 100 \text{ K}$. Below this temperature, formation of H_2 is most efficient.

$\text{H}^+/\text{H}/\text{H}_2$: We show the $\text{H}^+/\text{H}/\text{H}_2$ transition in Fig. 2. While in an UV dominated chemistry the H^+ is produced by cosmic ray ionization or by charge exchange with O^+ , X-rays are able to efficiently ionize hydrogen through ionization by photoelectrons and produce ionization fractions as large as $x_e \sim 1$. In the low density region of the disk, hydrogen is completely ionized, because the gas is directly exposed to X-rays, and the recombination rates are relatively slow due to the low densities ($n_{\text{H}} < 10^3 \text{ cm}^{-2}$) and high temperatures $T > 5000 \text{ K}$. This is followed by a transition layer dominated by atomic hydrogen, but where the abundance of $x_{\text{H}^+} \sim 10^{-4}$ and $x_{\text{H}_2} \sim 10^{-2}$. This is an active layer, where transient species, such as OH^+ and H_2O^+ , are highly abundant (see Fig. 4). H_2 is dominant in the shielded part of the disk, when dust temperatures are below $T \sim 100 \text{ K}$. Note that the H_2 formation efficiency drops rapidly at $T_{\text{dust}} > 100 \text{ K}$ and is tiny when $T_{\text{dust}} > 1000 \text{ K}$. At these temperatures H_2 is formed through $\text{H}^- + \text{H} \rightarrow \text{H}_2 + e^-$, a route which is especially efficient when X-rays are present. The electron abundances drop below $x_e < 10^{-8}$ where H_2 is dominant. Interestingly, we see a sudden increase of the electron abundance with radius at $R \sim 6 \text{ pc}$. Beyond this radius water freezes out, and depletes oxygen from the gas-phase. The charge exchange reactions $\text{H}^+ + \text{O} \leftrightarrow \text{H} + \text{O}^+$ sets the ratio between O^+ and H^+ . When oxygen is depleted, H^+ will not be neutralized by this reaction resulting in

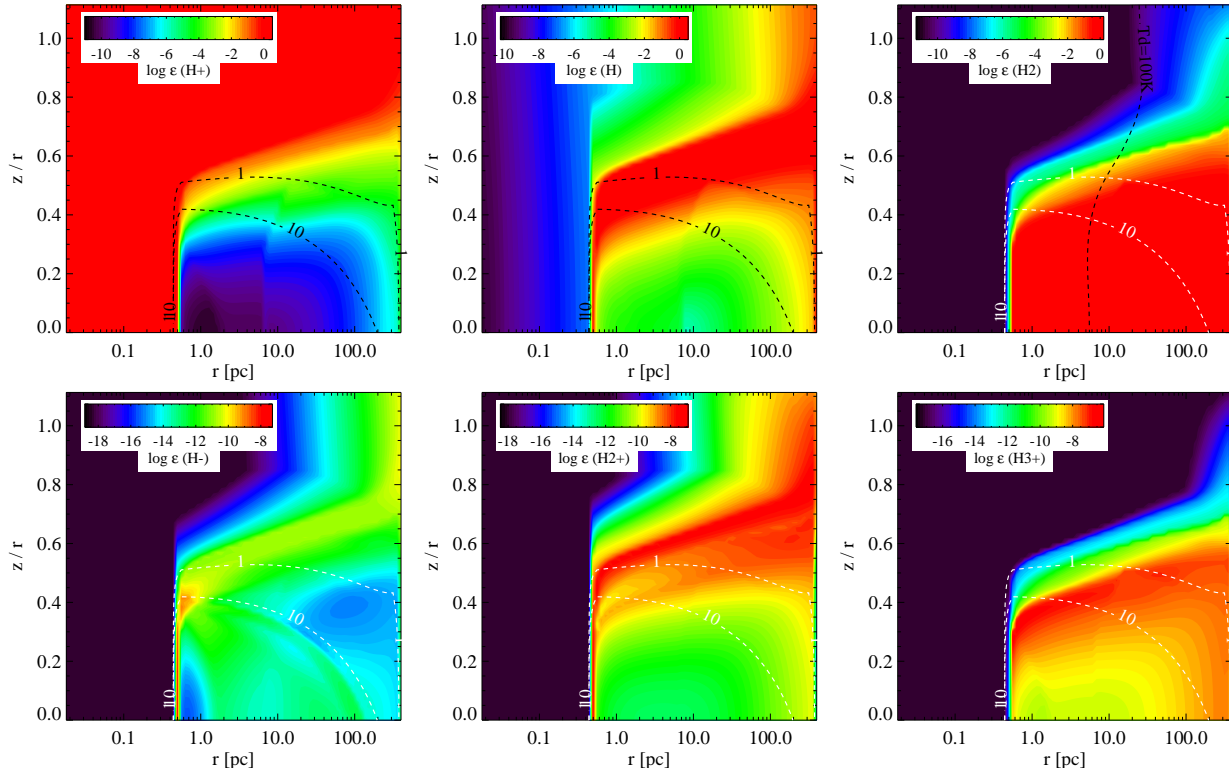


FIG. 2.— Abundances of H^+ , H , H_2 , H^- , H_2^+ and H_3^+ . Contours for $A_V = 1$ and 10 and $T_{\text{dust}} = 100$ K are overplotted.

a higher abundance x_{H^+} .

H^- , H_2^+ , and H_3^+ : H^- is abundant ($x_{\text{H}^-} > 10^{-10}$) at the transition from H^+ to H . At this location the formation of H^- is optimal, since there are many electrons available as well as neutral atomic hydrogen to allow $\text{H} + e^- \rightarrow \text{H}^- + \text{photon}$. Another region of the disk where H^- abundances are high ($x_{\text{H}^-} \sim 10^{-13}$) is for optical extinction $A_V > 10$ mag, in which case the interstellar radiation field is not able to destroy H^- efficiently. Slightly beyond the region where the H^- abundance is highest, there is a layer with a high H_2^+ abundance ($x_{\text{H}_2^+} \sim 10^{-8}$). At this location, the temperature is high enough to allow for the radiative association reaction $\text{H}^+ + \text{H} \rightarrow \text{H}_2^+ + \text{photon}$. Another maximum occurs where the transition from H to H_2 occurs, and then H_2^+ is formed by X-ray and cosmic ray ionization. When the full transition to H_2 has occurred, the H_2^+ abundance drops, since it is transformed into H_3^+ through the $\text{H}_2^+ + \text{H}_2 \rightarrow \text{H}_3^+ + \text{H}$.

$\text{C}^+/\text{C}/\text{CO}$: Carbon is ionized to high ionization states high up in the disk and at small radii ($r < 0.5$ pc). The code allows the species to be doubly ionized, and the double ionized species serve as a sink species, and therefore most carbon is in C^{2+} . Charge transfer reactions for three or more times ionized species are fast (Butler & Dalgarno 1980), and generally orders of magnitude larger than those for singly and doubly ionized species. Therefore, the fact that we only include doubly ionized species is a reasonable approximation, since highly ionized species are quickly reduced back to a doubly ionized state. Fig. 3 shows the abundances of C^+ , C , and CO , which are commonly observed in active galaxies. Although there is a transition from C^+ , to C and CO ,

the structure is much more complex than in the case of hydrogen. C^+ is most abundant in the upper layers of the disk, and the highest abundances of C^+ are coinciding with the atomic hydrogen layer. This C^+ shows a minimum in the middle of this layer, which is caused by a number of competing reactions. The abundance of H_2 increases over the layer, and makes the endothermic reaction $\text{C}^+ + \text{H}_2 \rightarrow \text{CH}^+ + \text{H}$ possible. As the temperature drops toward the mid-plane, this reaction becomes less efficient, and the C^+ abundance increases again. CO is most abundant between radii $r \sim 0.5 - 9$ pc. Beyond these radii, water is almost fully frozen out, which depletes the gas phase oxygen abundance entirely, and prevents the formation of CO in the gas phase. The timescales for freezing out water are very long, and given the occurrence of supernova and cloud-cloud collisions that remove molecules from the icy mantles, it is not expected that the CO entirely freezes out. Also, the size of the molecular disk in the low ($J = 1 - 0$ and $J = 2 - 1$) CO transitions show that the disk is extended beyond ~ 10 pc, as discussed earlier. This implies that a time-dependent treatment of the chemistry is required.

O , OH , H_2O , OH^+ , H_2O^+ , and H_3O^+ : Fig. 4 shows the oxygen related species. Neutral oxygen is the most abundant in those regions of the disk where temperatures are $T < 5000$ K, and above the temperature where H_2O freezes out. H_2O freezes out on grain surfaces when dust temperatures are below $T \sim 90 - 110$ K. This process removes oxygen from the gas phase, which also affects other species (e.g., CO and H_2). H_2O has an abundance of 10^{-4} with respect to H_2 in the dense ($n_{\text{H}} > 10^7 \text{ cm}^{-3}$) warm ($T_{\text{gas}} \sim 300 - 1000$ K) part of the disk, between 0.5 and 2.0 pc, although water remains present at lower abundances in the more shielded part of the disk, until

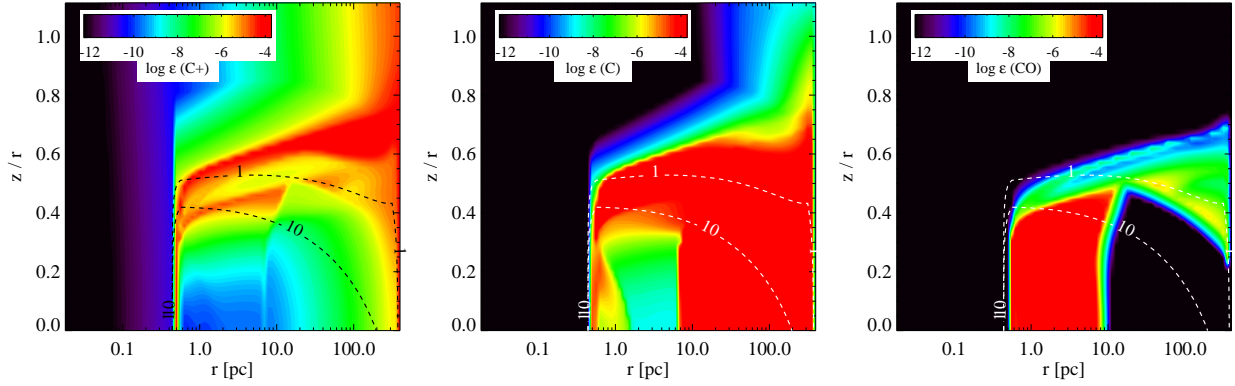


FIG. 3.— Abundances of C^+ , C, and CO. Contours for $A_V = 1$ and 10 are overlotted.

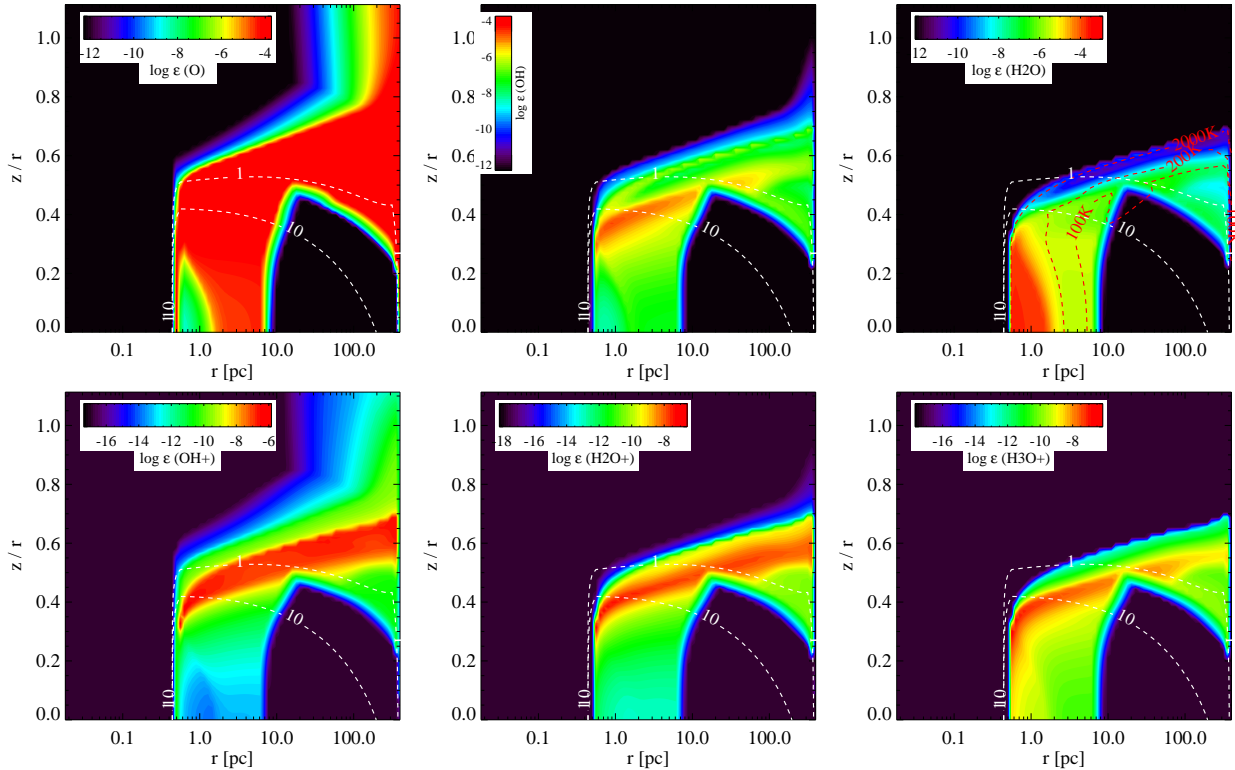


FIG. 4.— Abundances of O, OH, H_2O , OH^+ , H_2O^+ and H_3O^+ . Contours for $A_V = 1$ and 10 and $T_{\text{gas}} = 100, 200,$ and 2000 K are overlotted.

it freezes out. In the warm dense, neutral ($x_e < 10^{-8}$) parts of the disk, H_2O is formed through neutral-neutral reactions, while in the regions of the disk where densities are low, and ionization fractions of order $x_e \sim 10^{-4}$, it is also formed through ion-molecule reactions $H^+ + O \rightarrow O^+ + H$, $O^+ + H_2 \rightarrow OH^+ + H$, $OH^+ + H_2 \rightarrow H_2O^+ + H_2$, $H_2O^+ + H_2 \rightarrow H_3O^+ + H_2$, followed by $H_3O^+ + e^- \rightarrow H_2O + H$. In that particular part of the disk, we see a clear transition zone from OH^+ to H_2O^+ to H_3O^+ .

N^+ , HCN and HCO^+ (Fig. 5): HCN and HCO^+ are commonly observed by ground-based telescopes and trace dense ($n_H > 10^4 - 10^5 \text{ cm}^{-3}$) gas. Extra-galactic N^+ has been recently observed by the Herschel Space Telescope (van der Werf et al. 2010; Loenen et al. 2010) and also in the high-redshift universe. N^+ is very abundant in the transition layer from ionized to atomic hydrogen. HCO^+ is entirely depleted in the water freeze-out

zone. HCN, on the contrary, has abundances in those regions that are $x_{\text{HCN}} \sim 10^{-8} - 10^{-6}$. HCN is most abundant in the warm dense parts of the disk, following the abundance structure of water. HNC, which is also commonly observed, follows the abundance structure of HCN at $T < 100$ K. Interestingly, there is an endothermic reaction $H + HNC \rightarrow HCN + H$, that efficiently converts HNC into HCN. Including additional lines from HNC in the analysis would thus help constraining the temperature of the dense gas.

3.2. Chemical relaxation timescales and the need for a time-dependent solution

The chemical relation time (Woitke et al. 2009) is defined as:

$$\tau_{\text{chem}} = \max_{\text{valid } n} |Re\{\lambda_n\}^{-1}|, \quad (1)$$

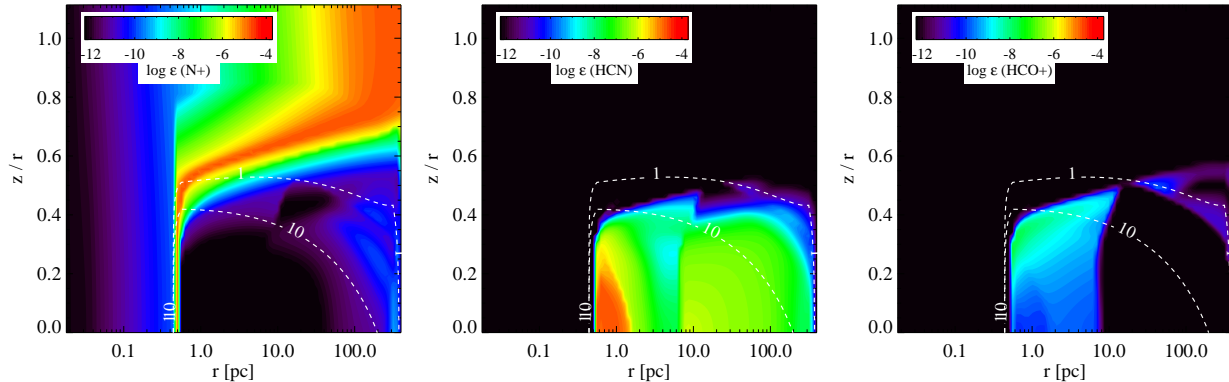


FIG. 5.— Abundances of N^+ , HCN, and HCO^+ . Contours for $A_v = 1$ and 10 are overplotted.

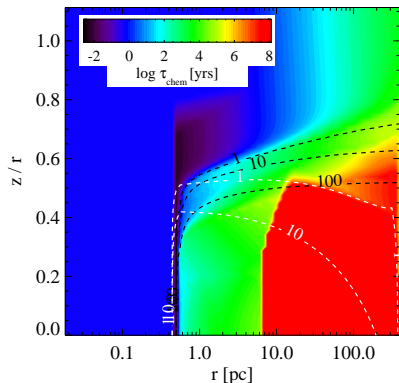


FIG. 6.— Chemical relaxation timescale for a disk in thermal and chemical equilibrium. Contours for $A_v = 1$ and 10, as well as $\tau(1\text{keV}) = 1, 10$ and 100 are overplotted.

where λ_n are the valid eigenvalues of the chemical Jacobian $\delta F_i / \delta n_j$. Chemical relaxation timescales in the regions of the disk where freeze out occurs are of the order of $\tau_{\text{chem}} \sim 1$ to 100 Myrs (see Fig. 6). This was already pointed in earlier work (Bergin et al. 2000), where it was shown that CO can be depleted from the gas phase on a timescale $\tau_{\text{depl}} > 10^6$ yrs. This happens through CO destruction by He^+ , after which oxygen is locked into H_2O . They included in this work also the formation of water on grains ($\text{O}(\text{grain}) \rightarrow \text{H}_2\text{O}(\text{grain})$), without allowing it to return into the gas-phase. This is true for grains that have already an icy layer, but for bare grains, a significant (a fraction of 0.5 to 0.6 for H_2O) amount will be desorb from the grain into the gas phase upon formation (Meijerink et al. 2012b). Accreted oxygen will not necessarily remain on the grain. As mentioned in the introduction, the chemical relaxation timescales are larger than the dynamical and supernova timescales, which are typically $\tau_{\text{dyn}} < 0.1 - 1$ Myr, and are removing molecules from the grain.

In order to study the effect of time-dependent freeze-out on the chemistry, we take the model described in the previous section, but without any molecules frozen out onto grains. The initial conditions are thus fully molecular, which we expect for ULIRGs. One exception is the gas that is directly exposed to radiation. Then the gas is partly atomic/ionized or even fully ionized (see equilibrium solution described in previous section). We consequently add the possibility that the molecules CO, H_2O , CH_4 , CO_2 , and NH_3 can freeze-out onto grains. No surface reactions are involved into the current calcu-

lation, and therefore the oxygen depletion timescale is possibly overestimated, as oxygen is not accreted onto the grain and reacting to OH and H_2O . We expect however that most of these species are entering the gas-phase upon formation, since they are forming on mostly bare grains. The current version of the ProDiMo code allows the evolution of the chemistry for a given gas and dust temperature structure. In the results we show below, we take the gas and dust temperature from the equilibrium solution, and evolve the chemistry for 100 Myrs. We checked the differences in the thermal balance between the equilibrium model and the starting conditions for the time-dependent model and the changes are marginal, and only present in a small fraction of the disk.

3.3. Effect on the chemical structure of commonly observed molecules

We concentrate on the species that are affected by time-dependent chemistry. The effect of oxygen depletion on the hydrogen species are marginal, and the abundance structures do not significantly differ from the equilibrium solution, and are therefore not discussed here.

C⁺, C, CO, and CO ice: Fig. 7 shows the abundance structure of C^+ , C, CO, and CO ice abundances at time $t = 10^4, 10^6, \text{ and } 10^8$ yrs compared to the equilibrium solution. The C^+ abundance structure shows a thick layer with $x_{C^+} \sim 10^{-4}$ at all times, similar to the equilibrium solution. The second deeper-lying layer, however, is not interrupted at early times. The interruption of this second layer, that occurs in the equilibrium solution due to the freeze-out effects, starts to show at $t > 10^6$ yrs. At $t = 10^4$ yrs, the neutral carbon abundance structure shows high ($x_C \sim 10^{-4}$) abundances down to the mid-plane at both the inner edge of the disk and at $R > 100$ pc, while CO has abundance $x_{\text{CO}} \sim 10^{-4}$ in the entire disk up to $R \sim 300$ pc, and $z/R \sim 0.4$. Over time, neutral carbon becomes more abundant, and at $t = 10^8$ yrs, the radius beyond which carbon is dominant at the mid-plane moved from $R \sim 100$ pc to 5 pc, while the CO abundance slowly drops. Compared to the equilibrium model, the CO is not completely depleted from the gas-phase, and still has significant abundances out to $R \sim 300$ pc at $t = 10^8$ yrs. We also find that a small abundance ($x_{\text{COice}} < 10^{-12}$) of CO ice is developing on the grains. The fraction of CO ice compared to gas phase CO is orders of magnitude smaller.

O, OH, and H₂O (Fig. 8): Oxygen starts to get affected at $t > 10^6$ years. It only drops below an

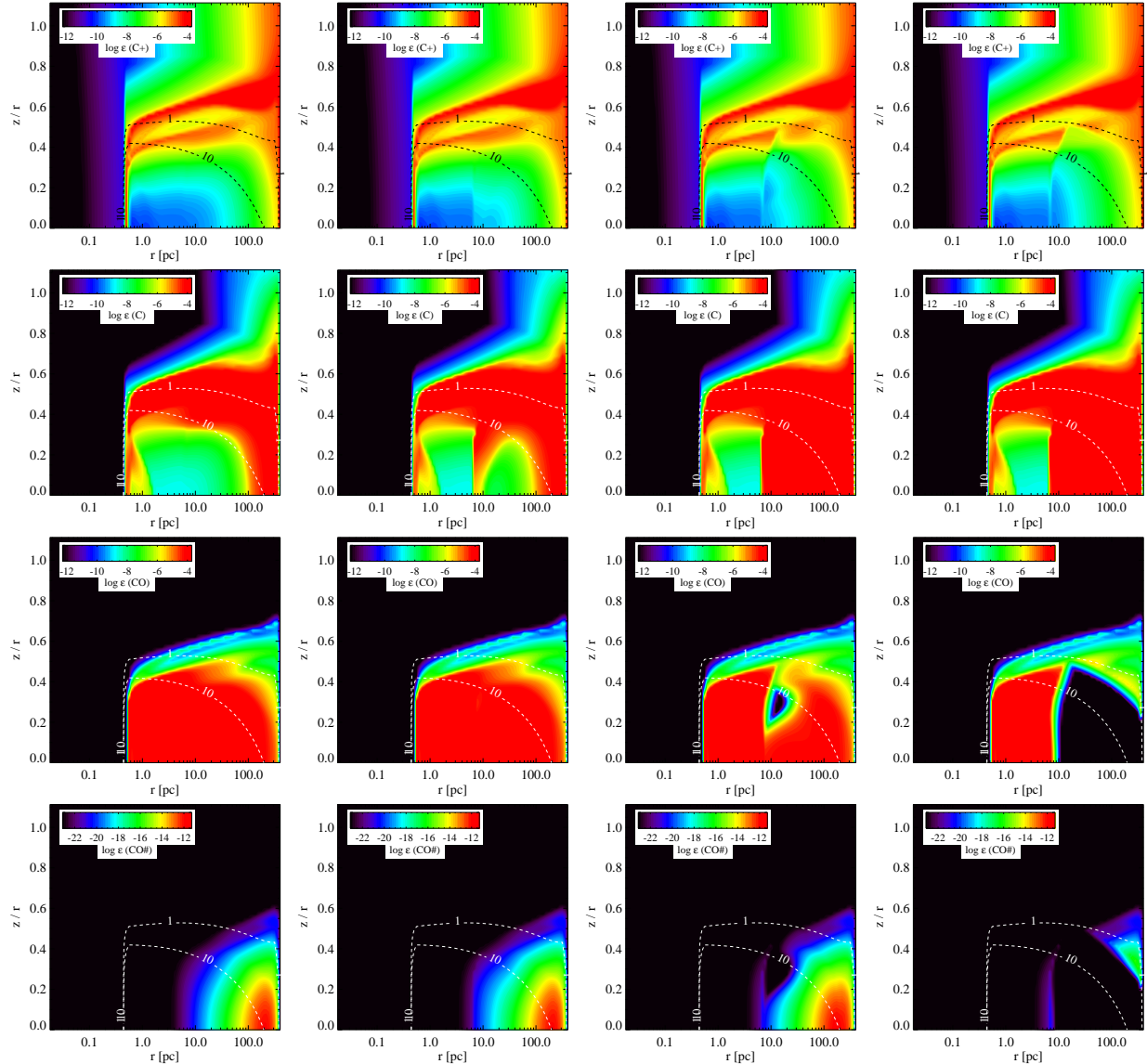


FIG. 7.— Chemical abundances of C^+ (top), C, CO and CO ice (bottom) from the time-dependent solution at time $t = 10^4$, 10^6 , and 10^8 years (left), and the equilibrium solution (right). Contours for $A_V = 1$ and 10 are overplotted.

abundance $x_O < 10^{-12}$ in a small part of the disk at $t = 10^8$ yrs, while the region where oxygen is below $x < 10^{-6}$, spans from $R = 5 - 30$ pc and $z/R = 0 - 0.4$. Overall, the time-dependent oxygen abundance structure does not show the prominent freeze-out region as in the case of the equilibrium model. The OH abundance shows an interrupted layer with a maximum abundance $x_{OH} \sim 10^{-5}$ in the equilibrium model, which is due to freeze-out. This interruption is not present at early times $t < 10^6$ yrs. Although it starts to show at $t = 10^8$ yrs, it is not as prominent as in the equilibrium model. The OH is slowly being depleted from the gas phase, but it only drops below $x_{OH} < 10^{-12}$ in a small fraction of the molecular part of the disk, similar to oxygen. H_2O is very abundant at the inner rim ($x_{H_2O} \sim 10^{-4}$), but also shows abundances $x > 10^{-6}$ in large parts of the disk, where gas temperatures are less favorable for water formation. Similar to oxygen and OH, H_2O is slowly depleted from the gas phase, but there are still significant abundances out to $R \sim 300$ pc after $t = 10^8$ yrs.

The water ice fraction is slowly increasing over time at $R > 5$ pc. However, after $t = 10^8$ yrs, the region where H_2O ice abundance exceeds $x_{H_2O\text{ice}} > 10^{-4}$ is not as extended as in the equilibrium model ($R \sim 100 - 200$ pc compared to $R = 400$ pc).

OH^+ , H_2O^+ , and H_3O^+ : Similar to OH, OH^+ , H_2O^+ and H_3O^+ have a continuous layer of maximum abundance in the upper part of the disk at $t = 10^4$ yrs: The interruption of these layers by freeze-out effects is not present at $t = 10^4$ yrs as is the case in the equilibrium model. When time is progressing and H_2O is slowly being depleted onto grains, the freeze-out also affects the ionic species and, as a result, the high-abundance layer is slowly being affected (OH^+ and H_2O^+) or even interrupted (H_3O^+) at $t = 10^8$ yrs. Since the water is not completely frozen-out in the regions with $T < 90 - 110$ K, the ionized water-related species still have very significant abundances at radii $R > 7$ pc.

N^+ , HCN , and HCO^+ : N^+ settles very quickly to a stable abundance structure, contrary to HCN and

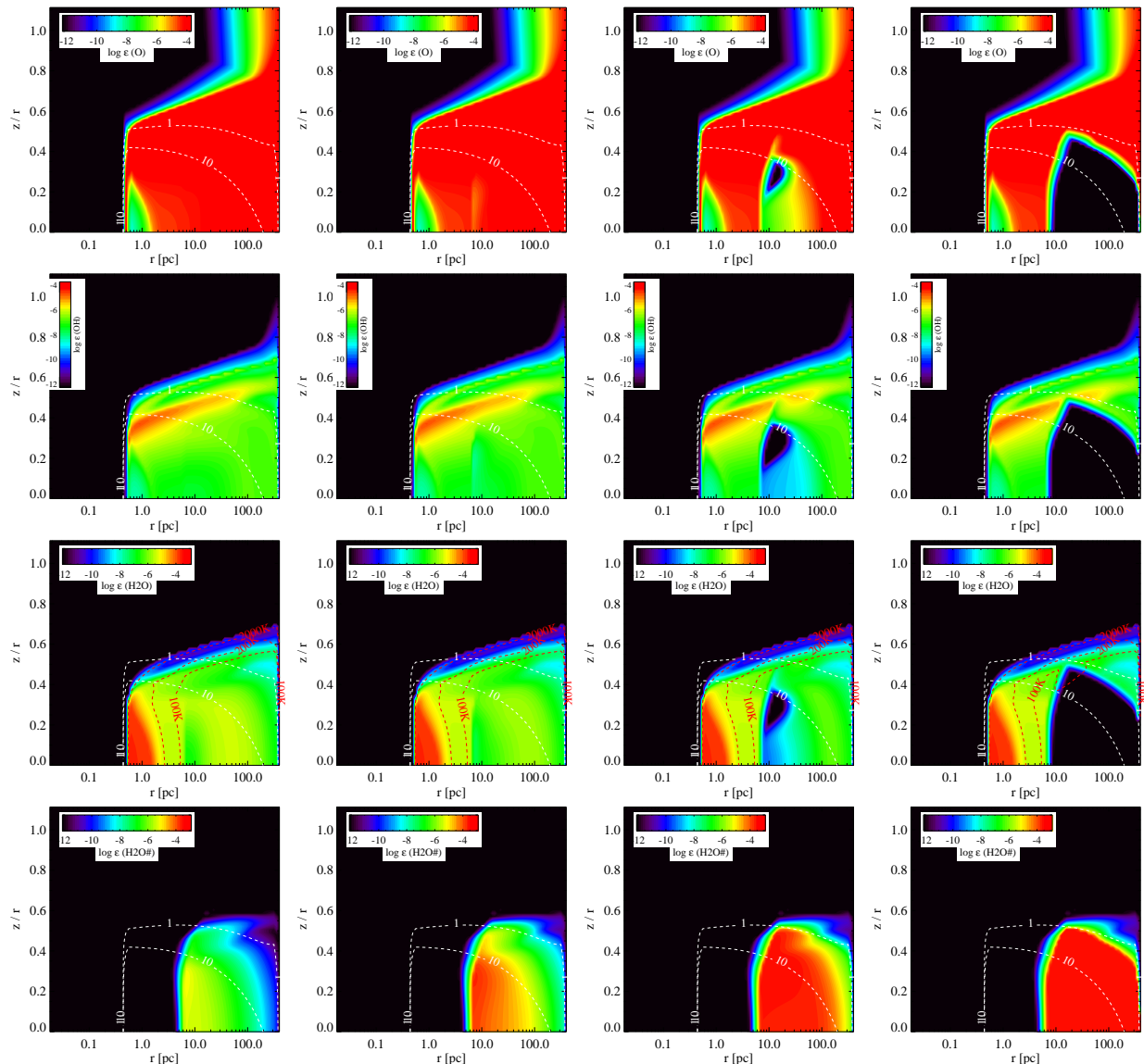


FIG. 8.— Chemical abundances of O (top), OH, H₂O, and H₂O ice (bottom) from the time-dependent solution at time $t = 10^4$, 10^6 , and 10^8 years (left), and the equilibrium solution (right). Contours for $A_V = 1$ and 10 and temperature $T = 100$, 200 and 2000 K are overplotted.

HCO⁺. Only where abundances are relatively small ($x_{N^+} \sim 10^{-12}$) in the outer region of the AGN torus and below $z/R < 0.4$, the N⁺ shows some fluctuations over time, which are a consequence of freeze-out effects. Where oxygen is slowly being depleted from the gas phase chemistry due to H₂O freeze out, the HCN abundance is slowly increasing from $x_{\text{HCN}} \sim 10^{-9}$ ($t = 10^4$ yrs) to 10^{-7} ($t = 10^8$ yrs). The solution is very similar to the equilibrium solution, although the HCN abundance in the region where water freezes out is lower by a factor 3-10. HCO⁺ is abundant throughout the disk, when no water is frozen out, and is slowly depleted with time. Contrary to the equilibrium model, HCO⁺ is still present at the level $x_{\text{HCO}^+} \sim 10^{-10}$ in the freeze-out zone after 100 million years.

4. EFFECTS OF TIME DEPENDENT CHEMISTRY

4.1. Total masses of atomic and molecular species

The masses of the discussed atomic and molecular species for the time-dependent ($t = 10^4$, 10^6 , and 10^8 yrs) and equilibrium model are listed in Table 1. The hydrogen species (H, H₂, H⁺, H₂⁺, and H₃⁺) are not affected by oxygen depletion, and show constant mass fractions over time. The same is the case for C⁺ and N⁺ that are produced in the ionized/atomic part of the AGN disk. This is contrary to the total mass of neutral carbon, that is increasing with time. After 100 million years, it is still a factor of two lower than the mass resulting from the equilibrium model. For CO the difference is even larger, but contrary to C, the CO mass is decreasing with time. The CO mass is more than a factor 10 higher in the time-dependent model after 100 million years. The amount of CO ice is almost negligible, but note that in the time-dependent model, the CO ice mass is 5 orders of magnitude higher. Atomic oxygen is also depleted over time, but similar to gas-phase CO, the mass in atomic hydrogen is much higher than the equilibrium model. Af-

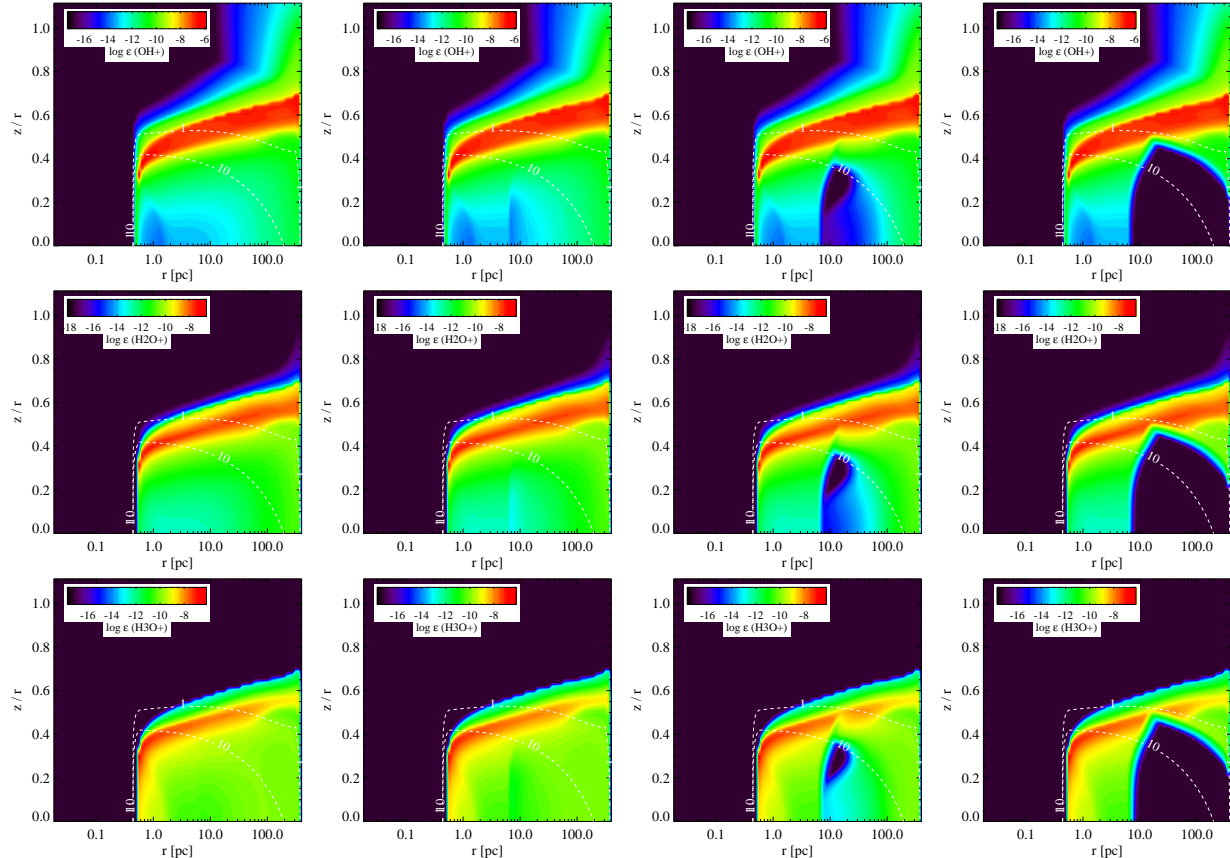


FIG. 9.— Chemical abundances of OH^+ (top), H_2O^+ (middle), and H_3O^+ (bottom) from the time-dependent solution at time $t = 10^4$, 10^6 , and 10^8 years (left), and the equilibrium solution (right). Contours for $A_V = 1$ and 10 are overplotted.

TABLE 1
TOTAL MASSES IN THE DISK OF ATOMIC AND MOLECULAR SPECIES

Species	Mass [M_\odot]			
	10^4 yrs	10^6 yrs	10^8 yrs	Equil.
H	8.0(7)	8.0(7)	8.0(7)	8.0(7)
H_2	6.9(8)	6.9(8)	6.9(8)	6.9(8)
H^-	2.4(-3)	2.4(-3)	2.4(-3)	2.4(-3)
H^+	1.9(7)	1.9(7)	1.9(7)	1.9(7)
H_2^+	1.2(0)	1.2(0)	1.2(0)	1.2(0)
H_3^+	2.6(1)	2.6(1)	2.5(1)	2.6(1)
C^+	1.0(5)	1.0(5)	1.0(5)	1.0(5)
C	6.0(5)	6.0(5)	8.0(5)	1.7(6)
CO	1.1(6)	1.1(6)	6.8(5)	4.5(4)
CO ice	2.1(-3)	2.1(-3)	2.6(-3)	6.0(-8)
O	2.7(6)	2.7(6)	2.4(6)	6.6(5)
OH	1.9(3)	1.8(3)	1.4(3)	3.7(2)
H_2O	1.9(4)	1.5(4)	9.1(3)	5.7(3)
H_2O ice	2.6(3)	8.4(4)	8.6(5)	3.2(6)
OH^+	3.3(1)	3.3(1)	3.3(1)	3.3(1)
H_2O^+	2.3(0)	2.3(0)	2.3(0)	2.2(0)
H_3O^+	2.3(0)	2.2(0)	1.7(0)	8.6(-1)
N^+	6.6(3)	6.6(3)	6.6(3)	6.6(3)
HCN	7.0(2)	7.3(2)	1.4(3)	2.2(3)
HCO^+	1.5(0)	1.3(0)	6.9(-1)	1.7(-1)

ter 10^8 yrs, the atomic oxygen mass is a factor of 4 higher than the equilibrium model. Water is depleted by a factor 2 after 100 million years with respect to its initial mass, but a factor 2 higher than the equilibrium model. The amount of water ice reaches almost a million solar masses after 100 million years, which is a factor 4 below the equilibrium model.

HCN profits from oxygen depletion, and its mass increases by a factor 2 after 100 million years, which is still 30 percent lower than the equilibrium model. On the other hand, HCO^+ is slowly being depleted, and is reduced by 60 percent over time, but a factor 4 higher than equilibrium model. The mass ratio of HCN/HCO^+ is $\sim 10^4$ for the entire disk in the equilibrium model. On the other hand, the time-dependent HCN/HCO^+ mass ratio is smaller by more than an order of magnitude compared to the equilibrium model. This will have consequences for the observed line emission.

It is not very likely that clouds will survive for times as large as 10^8 yrs. Studies of star-forming regions in our galaxy showed that their ages range between 1 to 15 Myrs (Palla & Stahler 2000; de Geus et al. 1989; Webb et al. 1999; Mamajek et al. 1999). Ionic species, such as C^+ and N^+ , have reached equilibrium by that time. This is not the case for important molecular species, such as CO and H_2O . This strongly argues that the initial conditions chosen for the molecular cloud play an important role. The effect of the choice of initial conditions was investigated by starting with a partially ionized and partly atomic medium. Although this is probably not a very realistic initial state, it is illustrative to note that the mass evolution of several important species is severely altered. For example, the CO mass in the models with the molecular initial state decreases from $1.1 \times 10^6 M_\odot$ (10^4 yrs) to $6.8 \times 10^6 M_\odot$ (10^8 yrs), compared to 1.5×10^4 to $8.7 \times 10^5 M_\odot$ when starting with the ionic/atomic initial state. In both cases the C^+ mass is approximately constant over

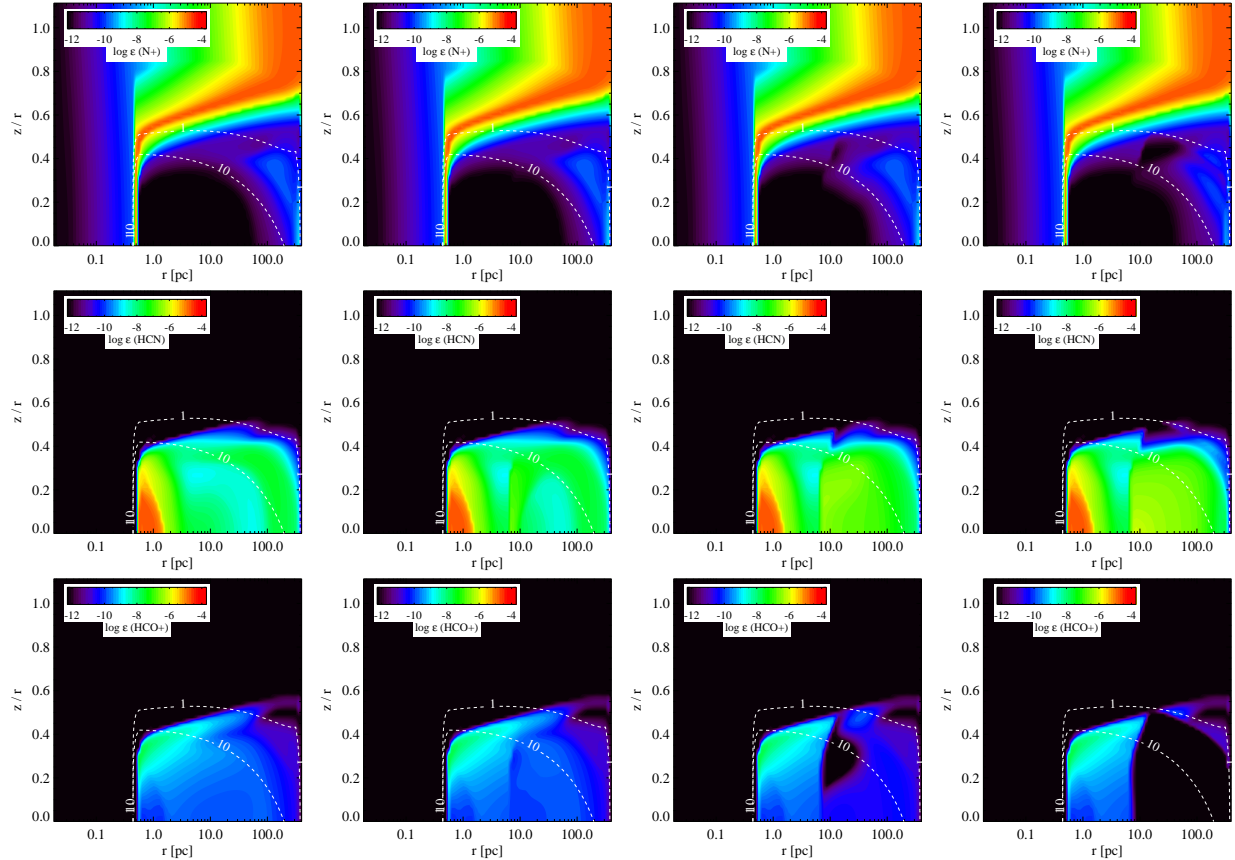


FIG. 10.— Chemical abundances of N^+ (top), HCN (middle), and HCO^+ (bottom) from the time-dependent solution at time $t = 10^4$, 10^6 , and 10^8 years (left), and the equilibrium solution (right). Contours for $A_V = 1$ and 10 are overplotted.

time ($10^5 M_\odot$), which results in a decreasing CO/C⁺ ratio for the molecular case and an increasing ratio for the ionic/atomic case. In both cases, the HCN mass increases with time, but the absolute mass is approximately a factor two higher at all times, when starting with molecular initial conditions. HCO^+ shows a similar behaviour as CO, and increases from 3.2×10^{-2} to $1.1 M_\odot$ in the ionic/atomic case, and decreases from 1.5 to $0.7 M_\odot$ in the molecular case. Although the behaviour is different, HCN/ HCO^+ mass ratio is always smaller in the time-dependent case for ages $\tau_{chem} > 10^4 - 10^5$ yrs than in the equilibrium case.

4.2. Consequences for observables

We calculated the line emission for a number of fine-structure lines and rotational transitions of CO, H_2O , HCN, and HCO^+ for a face-on disk and using an escape probability method (Table 2).

The [CII], [CI] and [OI] fine-structure lines are hardly affected over time, even though the [OI] and [CI] mass is varying over time. Both [OI] and [CI] are optically thick ($\tau > 100$ and 10, respectively) at those radii in which 90 percent of the emission is being produced. The line emission of CO in the time-dependent model is much larger than in the equilibrium model, between a factor 5 to 10, even after 100 million years. The CO line luminosities are much closer to the ones observed for Mrk 231 with Herschel (van der Werf et al. 2010). The water lines are also brighter in the equilibrium model, but they are not as much enhanced as the CO lines. The H_2O lines are

close to the equilibrium model after 100 million years.

The line ratios for the lowest ($J_{up} \leq 4$) rotational transitions of HCN and HCO^+ range between 2-10 (between $t = 10^4$ and 10^8 yrs), consistent with current observations of AGN, but still a factor of 2-4 higher. The time-dependent HCN/ HCO^+ line ratios agree better with values observed for galaxies with AGN. The latter range from 1-2 for $J = 1-0$ (Krips et al. 2008) and are slightly larger than 3 for $J = 4-3$ (Pérez-Beaupuits et al. 2009). This suggests that current HCN and HCO^+ observations of AGN disfavor a state that is characterized by complete chemical equilibrium. This conclusion even holds for two very different initial states. In a follow-up paper, line intensities for a larger parameter study will be presented for the diagnostic molecules identified above.

5. SUMMARY AND CONCLUSIONS

We presented a proof-of-concept for the time-dependent chemistry in an AGN. We found that the freeze-out of water is strongly suppressed for durations shorter than 100 Myr. This affects the bulk of the oxygen and carbon chemistry occurring in AGN. The commonly used AGN tracer HCN/ HCO^+ is strongly time-dependent, with ratios of order a few for dynamical times that are shorter than a million years. This suggests that high angular resolution ALMA observations, which probe the narrow-line region on scales smaller than 100 pc, can reveal the evolutionary state of an AGN as it evolves under strong fluctuations in the SMBH accretion rate. We should bare in mind though that the model results do

TABLE 2
LINE FLUXES FOR COMMONLY OBSERVED ATOMIC AND MOLECULAR SPECIES

Line	λ [μm]	Luminosity [L_{\odot}]			
		10^4	10^6	10^8	Equil.
CO $J = 1 - 0$	2600.76	2.4(6)	2.4(6)	2.3(6)	2.9(5)
CO $J = 2 - 1$	1300.40	1.4(7)	1.4(7)	1.3(7)	9.3(5)
CO $J = 3 - 2$	866.96	3.1(7)	3.1(7)	3.0(7)	1.2(6)
CO $J = 4 - 3$	650.25	4.7(7)	4.7(7)	4.5(7)	1.8(6)
CO $J = 5 - 4$	520.23	5.4(7)	5.4(7)	5.0(7)	2.7(6)
CO $J = 6 - 5$	433.56	5.0(7)	5.0(7)	4.4(7)	4.1(6)
CO $J = 7 - 6$	371.65	4.0(7)	4.0(7)	3.4(7)	5.9(6)
CO $J = 8 - 7$	325.23	3.3(7)	3.3(7)	2.9(7)	7.8(6)
CO $J = 9 - 8$	289.12	3.0(7)	3.0(7)	2.7(7)	9.9(6)
CO $J = 10 - 9$	260.24	2.9(7)	2.9(7)	2.6(7)	1.2(7)
CO $J = 11 - 10$	236.61	2.8(7)	2.8(7)	2.5(7)	1.4(7)
CO $J = 12 - 11$	216.93	2.7(7)	2.7(7)	2.4(7)	1.6(7)
CO $J = 13 - 12$	200.27	2.6(7)	2.6(7)	2.3(7)	1.7(7)
[OI] $^3P_1 - ^3P_2$	63.18	4.9(9)	4.9(9)	4.8(9)	4.8(9)
[OI] $^3P_0 - ^3P_1$	145.53	5.5(8)	5.5(8)	5.5(8)	5.5(8)
[CII] $^2P_{3/2} - ^2P_{1/2}$	157.74	2.8(9)	2.8(9)	2.8(9)	2.8(9)
[CI] $^3P_1 - ^3P_0$	609.14	1.2(8)	1.2(8)	1.3(8)	1.6(8)
[CI] $^3P_2 - ^3P_1$	370.42	2.5(8)	2.5(8)	2.7(8)	4.2(8)
p-H ₂ O $1_{11} - 0_{00}$	269.27	2.8(7)	2.4(7)	1.0(7)	5.9(6)
p-H ₂ O $2_{02} - 1_{11}$	303.46	1.6(7)	1.3(7)	4.2(6)	3.9(6)
p-H ₂ O $2_{11} - 2_{02}$	398.64	8.9(6)	7.1(6)	3.5(6)	3.5(6)
p-H ₂ O $2_{20} - 2_{11}$	243.97	1.1(7)	8.5(6)	6.2(6)	6.2(6)
o-H ₂ O $3_{12} - 3_{03}$	273.19	7.9(6)	6.6(6)	5.4(6)	5.4(6)
o-H ₂ O $3_{21} - 3_{12}$	257.79	8.6(6)	7.7(6)	7.1(6)	7.1(6)
p-H ₂ O $4_{22} - 4_{13}$	248.25	4.3(6)	4.2(6)	4.2(6)	4.2(6)
o-H ₂ O $5_{23} - 5_{14}$	212.53	4.1(6)	4.1(6)	4.1(6)	4.1(6)
[NII] $^3P_1 - ^3P_0$	205.24	9.6(8)	9.6(8)	9.6(8)	9.6(8)
HCO ⁺ $J = 1 - 0$	3361.33	2.8(4)	2.7(4)	1.6(4)	2.8(3)
HCO ⁺ $J = 4 - 3$	840.38	3.4(5)	3.1(5)	1.8(5)	1.4(5)
HCN $J = 1 - 0$	3382.46	7.7(4)	8.0(4)	1.8(5)	1.8(5)
HCN $J = 4 - 3$	845.66	6.6(5)	7.4(5)	2.0(6)	4.6(6)

depend on the initial chemical state of the clouds. Especially the absolute mass of the diagnostic species are affected by this, and to a lesser extent also the mass ratios of the species. In order to test whether a result is robust, one should explore a range of possible initial states. We also note that the AGN torus is a clumpy medium with likely a complicated velocity field. This implies that clouds will also see attenuation variations on time-scales $\tau < 10^6$ yrs at radii $R < 100$ pc from the center. These effects are beyond the scope of this paper, but should be investigated carefully as well.

Strong evolutionary trends, occurring on time scales of $10^4 - 10^8$ years, are also found in species like, H₃O⁺,

CO, and H₂O. These species reflect, respectively, time dependent effects in the ionization balance, the transient nature of the production of molecular gas as traced by the X-factor, and the freeze-out/sublimation of water (key to much of the grain surface chemistry).

In closing, we note that an accurate representation of AGN chemistry requires time dependence. As a next step to the work presented here, to be pursued in a follow-up paper, it is necessary to calculate the response of the disk's thermal structure to radiative and hydrodynamic events and to compute line intensity maps for the diagnostic species identified above.

REFERENCES

- Ádámkóvics, M., Glassgold, A. E., & Meijerink, R. 2011, *ApJ*, 736, 143
Aresu, G., Meijerink, R., Kamp, I., et al. 2012, *A&A*, 547, A69
Bergin, E. A., Melnick, G. J., Stauffer, J. R., et al. 2000, *ApJ*, 539, L129
Butler, S. E., & Dalgarno, A. 1980, *ApJ*, 241, 838
de Geus, E. J., de Zeeuw, P. T., & Lub, J. 1989, *A&A*, 216, 44
Downes, D., & Solomon, P. M. 1998, *ApJ*, 507, 615
Draine, B. T. 1978, *ApJS*, 36, 595
Glassgold, A. E., Najita, J., & Igea, J. 2004, *ApJ*, 615, 972
González-Alfonso, E., Fischer, J., Isaak, K., et al. 2010, *A&A*, 518, L43+
Krips, M., Neri, R., García-Burillo, S., et al. 2008, *ApJ*, 677, 262
Loenen, A. F., van der Werf, P. P., Güsten, R., et al. 2010, *A&A*, 521, L2
Lutz, D., Maiolino, R., Spoon, H. W. W., & Moorwood, A. F. M. 2004, *A&A*, 418, 465
Maloney, P. R., Hollenbach, D. J., & Tielens, A. G. G. M. 1996, *ApJ*, 466, 561
Mamajek, E. E., Lawson, W. A., & Feigelson, E. D. 1999, *PASA*, 16, 257
Meijerink, R., Aresu, G., Kamp, I., et al. 2012a, *A&A*, 547, A68
Meijerink, R., Cazaux, S., & Spaans, M. 2012b, *A&A*, 537, A102
Meijerink, R., & Spaans, M. 2005, *A&A*, 436, 397
Meijerink, R., Spaans, M., & Israel, F. P. 2007, *A&A*, 461, 793
Palla, F., & Stahler, S. W. 2000, *ApJ*, 540, 255
Papadopoulos, P. P., van der Werf, P., Xilouris, E., Isaak, K. G., & Gao, Y. 2012, *ApJ*, 751, 10
Pérez-Beaupuits, J. P., Spaans, M., van der Tak, F. F. S., et al. 2009, *Astronomy & Astrophysics*, 503, 459
Pérez-Beaupuits, J. P., Wada, K., & Spaans, M. 2011, *ApJ*, 730, 48
Spaans, M. 1996, *A&A*, 307, 271
Tilling, I., Woitke, P., Meeus, G., et al. 2012, *A&A*, 538, A20

van der Werf, P. P., Isaak, K. G., Meijerink, R., et al. 2010, A&A, 518, L42
Wada, K., Papadopoulos, P. P., & Spaans, M. 2009, ApJ, 702, 63

Webb, R. A., Zuckerman, B., Platais, I., et al. 1999, ApJ, 512, L63
Woitke, P., Kamp, I., & Thi, W.-F. 2009, A&A, 501, 383
Woitke, P., Riaz, B., Duchêne, G., et al. 2011, A&A, 534, A44